# A cell-autonomous requirement for neutral sphingomyelinase 2 in bone mineralization

Zohreh Khavandgar,[1] Christophe Poirier,[4] Christopher J. Clarke,[5] Jingjing Li,[2] Nicholas Wang,[2] Marc D. McKee,[1,3] Yusuf A. Hannun,[5] and Monzur Murshed[1,2]

[1]Faculty of Dentistry, [2]Department of Medicine, [3]Department of Anatomy and Cell Biology, McGill University, Montreal, Quebec QC H3A 1A4, Canada
[4]Medical College of Georgia, Augusta, GA 30912
[5]Medical University of South Carolina, Charleston, SC 29425

A deletion mutation called *fro* (*fragilitas ossium*) in the murine *Smpd3* (*sphingomyelin phosphodiesterase 3*) gene leads to a severe skeletal dysplasia. *Smpd3* encodes a neutral sphingomyelinase (nSMase2), which cleaves sphingomyelin to generate bioactive lipid metabolites. We examined endochondral ossification in embryonic day 15.5 *fro/fro* mouse embryos and observed impaired apoptosis of hypertrophic chondrocytes and severely undermineralized cortical bones in the developing skeleton. In a recent study, it was suggested that nSMase2 activity in the brain regulates skeletal development through endocrine factors. However, we detected *Smpd3* expression in both embryonic and postnatal skeletal tissues in wild-type mice. To investigate whether nSMase2 plays a cell-autonomous role in these tissues, we examined the in vitro mineralization properties of *fro/fro* osteoblast cultures. *fro/fro* cultures mineralized less than the control osteoblast cultures. We next generated *fro/fro;Col1a1-Smpd3* mice, in which osteoblast-specific expression of *Smpd3* corrected the bone abnormalities observed in *fro/fro* embryos without affecting the cartilage phenotype. Our data suggest tissue-specific roles for nSMase2 in skeletal tissues.

## Introduction

ECM mineralization in bones and teeth is a genetically regulated process. In humans, genetic mutations may lead to a variety of diseases affecting ECM mineralization in skeletal and dental tissues, which include X-linked hypophosphatemia, hypophosphatasia, rickets, and some forms of osteogenesis/dentinogenesis imperfecta (Tanaka and Deluca, 1974; Whyte, 1994; Nesbitt et al., 1999; Glorieux et al., 2002; Goldberg et al., 2008). Although considered as a critical physiological process, the molecular mechanism of ECM mineralization is still not fully understood. Identification of novel genetic regulators of this process and elucidation of their modes of action may lead to effective interventions for genetic diseases associated with abnormal skeletal mineralization.

Our current understanding suggests that skeletal and dental ECM mineralization can be attributed to a large extent to the unique promineralization environment of these hard tissues. Two mineral ions, $P_i$ and calcium, when present at physiological concentrations, will promote apatitic mineral crystal growth within and between newly synthesized collagen fibrils in the skeletal ECM (Murshed et al., 2005). Apart from the mineral ions themselves, extracellular levels of mineralization inhibitors can also affect ECM mineralization (Luo et al., 1997; Okawa et al., 1998; Ho et al., 2000; Murshed et al., 2004). For example, >40 yr ago, it was shown that $PP_i$, a chemical derivative of $P_i$, can potently inhibit the mineralization process (Fleisch and Bisaz, 1962; Terkeltaub, 2001). More recently, it has been shown that matrix gla protein (MGP), a small extracellular protein, prevents ECM mineralization in the cartilage and vascular tissues (Luo et al., 1997; Murshed et al., 2004).

Type 1 collagen, a scaffolding ECM protein, and tissue-nonspecific alkaline phosphatase (ALPL [alkaline phosphatase, liver/bone/kidney]), an enzyme required for the cleavage of $PP_i$ in the bone matrix, are both necessary for normal bone mineralization (Waymire et al., 1995; Hessle et al., 2002; Murshed et al., 2005). We recently demonstrated the importance of these

Z. Khavandgar, C. Poirier, and C.J. Clarke contributed equally to this paper.

Correspondence to Monzur Murshed: monzur.murshed@mcgill.ca

Abbreviations used in this paper: MGP, matrix gla protein; micro-CT, microcomputed tomography; nSMase, neutral sphingomyelinase; qRT-PCR, quantitative real-time PCR; WT, wild type.



The Rockefeller University Press $30.00
J. Cell Biol. Vol. 194 No. 2 277–289
www.jcb.org/cgi/doi/10.1083/jcb.201102051

key determinants of ECM mineralization in an in vivo mouse model, in which *Alpl* forced expression in the dermis, a fibrillar, collagen-rich soft connective tissue, resulted in ectopic mineralization of the skin (Murshed et al., 2005). Although these findings established the concurrent requirements of a mineral-scaffolding protein matrix and phosphatase activities in skeletal ECM mineralization, they did not rule out the existence of other mechanisms working in concert to regulate this process. A recently identified mutation in a mouse model, which displays altered sphingolipid metabolism and poorly mineralized skeletal tissues, further enforces the likelihood that multiple mechanisms are involved in skeletal mineralization (Guenet et al., 1981; Aubin et al., 2005).

Although initially considered as inert structural molecules, sphingolipids are now recognized as important mediators for signal transduction pathways affecting various cell functions (Merrill et al., 1997; Milhas et al., 2010; Wu et al., 2010). Bone deformities in mouse models lacking a functional *Smpd3* (*sphingomyelin phosphodiesterase 3*) gene underscore the importance of sphingolipid metabolism in skeletal tissues (Aubin et al., 2005; Stoffel et al., 2005). *Smpd3* encodes neutral sphingomyelinase 2 (nSMase2), a membrane-bound enzyme, which cleaves sphingomyelin to generate the lipid second messenger ceramide. Ceramide generated by sphingomyelinases or by a de novo pathway affects a wide range of cellular processes, including cell death, proliferation, and differentiation (Obeid et al., 1993; Bose et al., 1995; Richard et al., 1996; Sanchez-Alavez et al., 2006).

In recent years, studies have provided useful perspectives on novel physiological roles for nSMase2 (Kolak et al., 2007; Rutkute et al., 2007; Tellier et al., 2007). Further insight into the functions of this enzyme came with the development of animal models lacking nSMase2 activity. Currently, there are two nSMase2-deficient mouse models available: one was generated by gene targeting ($Smpd3^{-/-}$), whereas the other carries a chemically induced deletion of 1,758 bp encompassing part of intron 8 and the adjacent exon 9 of the *Smpd3* gene (Aubin et al., 2005; Stoffel et al., 2005, 2007). The latter mutation known as *fragilitas ossium* or *fro* replaces the last 33 amino acids of nSMase2, resulting in a significant reduction of total neutral sphingomyelinase activities in the tissues of the *fro/fro* mice (Aubin et al., 2005; Stoffel et al., 2005, 2007). In their recent studies, Stoffel et al. (2005, 2007) characterized the skeletal phenotypes of the $Smpd3^{-/-}$ mice as a chondrodysplasia and speculated a systemic role for neuronal *Smpd3* in the regulation of the skeletal development. Although both the $Smpd3^{-/-}$ and *fro/fro* mutants show similar gross skeletal abnormalities, some phenotypic differences exist between these two models. For example, the skeletal phenotype appears to be milder in $Smpd3^{-/-}$ mice. Also, no bone or tooth mineralization defects were reported in this gene-targeted model. These differences raise the possibility that additional, as yet unknown, mutations in the chemically mutagenized *fro/fro* model may cause the severe skeletal abnormalities.

The goals of our current study were to characterize the skeletal phenotype of *fro/fro* mice and to investigate the local role of *Smpd3* in osteoblasts. Toward these goals, we performed a detailed characterization of the skeletal tissues in *fro/fro* embryos and adult mice using skeletal preparations, micro-computed tomography (micro-CT), and histology/histomorphometric analysis. We demonstrate here that the *fro* mutation affects bone ECM mineralization in both embryos and in adult mice and that there is a delay of apoptosis in the hypertrophic chondrocytes in the developing *fro/fro* skeleton. We also show that osteoblast-specific expression of the *Smpd3* transgene in *fro/fro;Col1a1-Smpd3* mice completely rescues the bone mineralization defects, whereas the cartilage phenotype that appears during early skeletal development remains unaffected. Our work establishes the *fro* mutation as the sole cause of skeletal abnormalities in the *fro/fro* mice and suggests a cell-autonomous, tissue-specific role for nSMase2 in the developing skeleton.

## Results

### Impaired bone mineralization in *fro/fro* mice

*fro/fro* neonates are characterized by a shortened body stature with skeletal abnormalities (Aubin et al., 2005). As shown by the skeletal preparations of the newborn mice, both flat (intramembranous) and long (endochondral) bones are affected—the parietal suture was poorly mineralized, whereas both fore- and hind limbs were severely bent in the *fro/fro* mutants (Fig. 1, A and B). Further analysis by micro-CT revealed a reduction of mineralized tissue in the flat bones of the skull and alveolar bones in the jaw (Fig. 1 C).

To further confirm that the observed decrease in mineralized tissue was attributable purely to a mineralization defect, we examined wild-type (WT) and mutant mice for the presence of excess osteoid, the proteinaceous matrix secreted by osteoblasts, which subsequently becomes mineralized. Histological analysis of the parietal bones in the skullcap of 2-d-old *fro/fro* mice revealed a severely hypomineralized matrix at the suture (Fig. 1 D, top). Also, there was a marked reduction of mineralization in the alveolar bones from these mice (Fig. 1 D, bottom). By 1 mo of age, the trabecular bones of *fro/fro* mice showed an increase of ∼5% in osteoid volume over total bone volume as measured by histomorphometry (Fig. 1, E and F). Similarly, there was a significant increase in the osteoid surface in the *fro/fro* bones (Fig. 1 G). These results indicate that osteoid ECM is indeed deposited but is not efficiently mineralized. None of these skeletal abnormalities were seen in *+/fro* mice; therefore, we used these mice as controls for our subsequent in vivo analyses.

### The *fro* mutation abolishes nSMase2 activity but does not affect its membrane localization

The *fro* mutation causes a deletion in *Smpd3*, resulting in a replacement of the last 33 amino acids of nSMase2. In a previous study, reduced nSMase activity was reported in skin samples collected from *fro/fro* mice (Aubin et al., 2005). This reduced enzymatic activity can be caused by a loss of the catalytic site and/or by impaired membrane targeting of the enzyme. To investigate this, we generated two FLAG-tagged expression constructs *CMV-Smpd3* and *CMV-mSmpd3* encoding the WT and a mutated nSMase2 that carries the *fro* mutation, respectively (Fig. 2, A and B). The constructs were used to transfect MCF-7

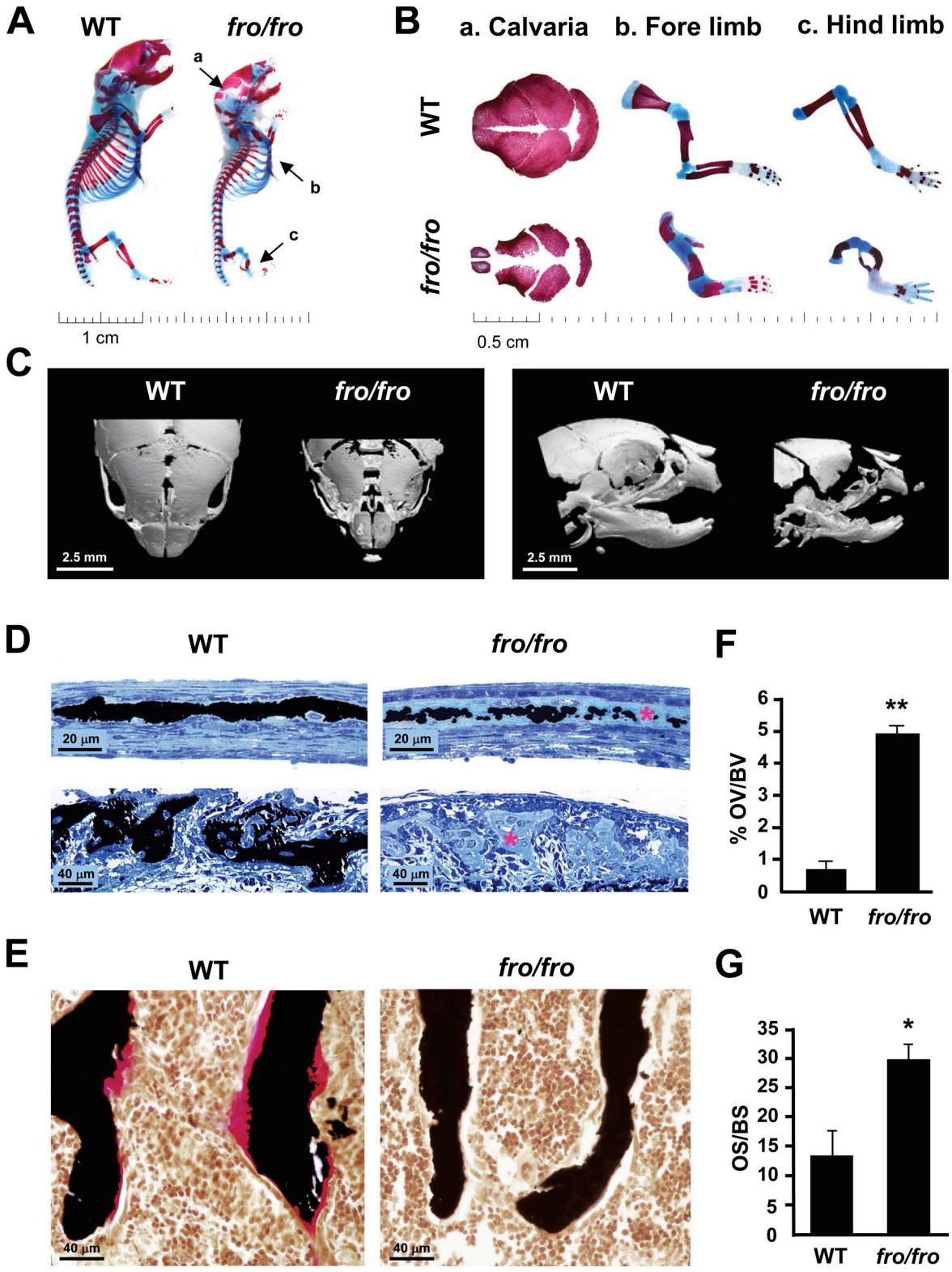


Figure 1. **Skeletal abnormalities in *fro/fro* mice.** (A and B) Alizarin red (stains mineralized tissues)– and Alcian blue (stains cartilage matrix)–stained skeletal preparations of 2-d-old wild-type (WT) and *fro/fro* mice showing hypomineralization of the calvaria (a) and short (b) and bent (c) fore- and hind limbs in the latter genotype. (C) Micro-CT analysis of 2-d-old WT and *fro/fro* heads confirming severe hypomineralization of various head skeletal elements as seen from the dorsal (left) and the lateral (right) views. (D) Light micrographs of von Kossa–stained mineral (black) in parietal (top) and alveolar bone (bottom) sections of a 2-d-old WT mouse and its *fro/fro* littermate. There is a marked decrease in mineralization, revealed by extensive areas of unmineralized osteoid (asterisks) in the *fro/fro* bones. (E) Von Kossa and van Gieson staining of vertebral bones from 1-mo-old WT and *fro/fro* littermates demonstrating a marked increase of unmineralized bone volume (pink staining) in the latter genotype ($n = 5$). (F and G) Comparison of the percentage of osteoid volume over total bone volume (OV/BV) and osteoid surface over bone surface (OS/BS) in WT and *fro/fro* mice ($n = 5$). Error bars represent standard deviations. *, $P < 0.05$; **, $P < 0.01$.

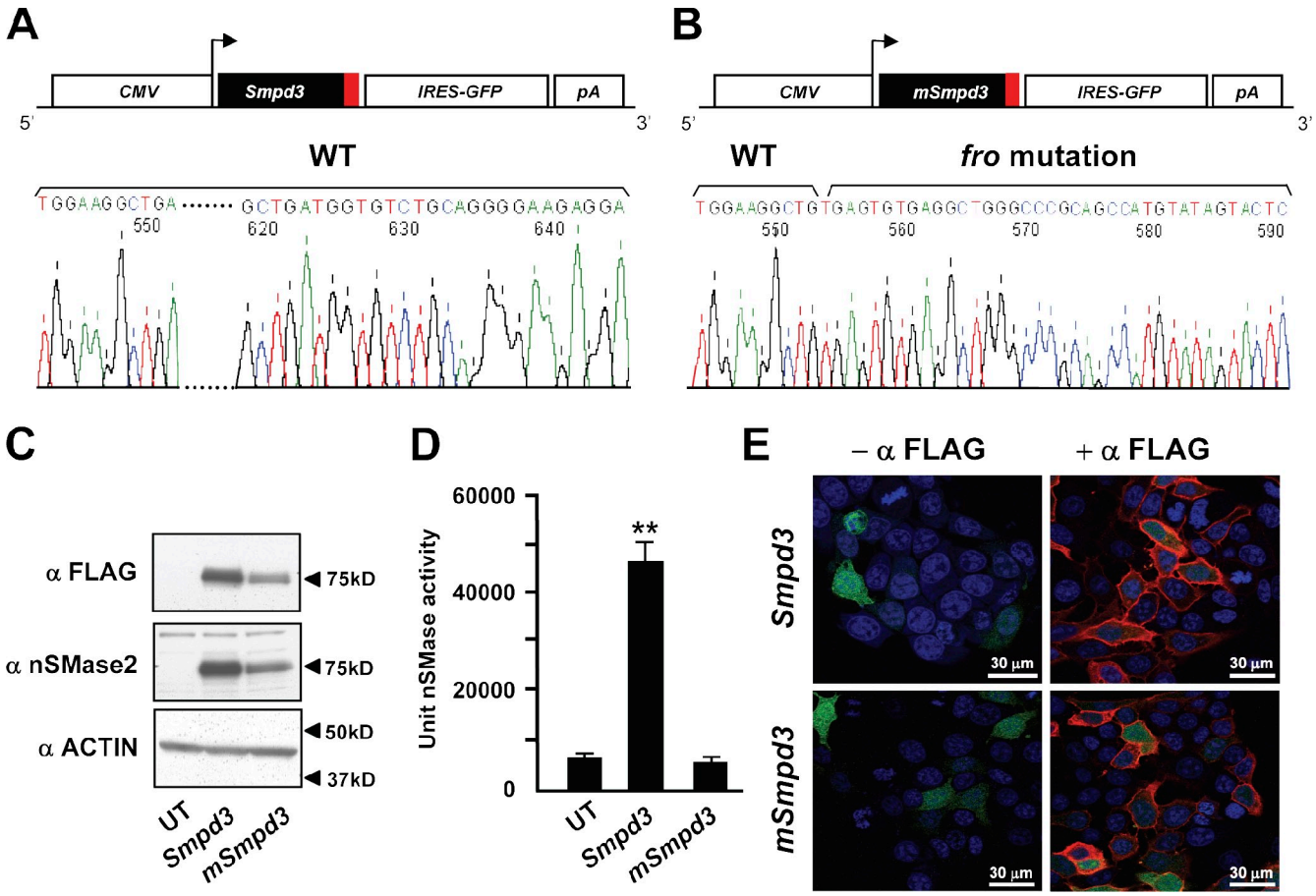


Figure 2. **Effects of *fro* mutation on nSMase2 activity and localization.** (A and B) Schematic depiction of WT (*Smpd3*; A) and mutant *Smpd3* (*mSmpd3*; carries *fro* mutation; B) expression constructs. The red boxes represent the FLAG coding sequence (CMV, cytomegalovirus promoter; IRES, internal ribosome entry site; and pA, SV40 polyadenylation signal). (C) Western blots showing expression of WT and mutant nSMase2 in transfected MCF-7 cells. FLAG-tagged proteins from the transfected cells were detected using an anti-FLAG (top) or an anti–mouse nSMase2 (middle) antibody. UT, untransfected. (D) A mixed micelle assay using $^{14}$C-labeled methyl-sphingomyelin shows that mutated nSMase2 does not have any nSMase activity. Error bars represent standard deviations. (E) Indirect immunofluorescence microscopy analyses showing comparable cell membrane localization of WT and mutated nSMase2 (shown in red) in transfected MCF-7 cells. The green and blue stains represent GFP localization and the nucleus, respectively. **, $P < 0.01$.

cells, and the expression of both WT and mutated proteins was confirmed by Western blotting (Fig. 2 C). As shown in Fig. 2 D, there was a marked increase in nSMase activity in cells transfected with *CMV-Smpd3* but not with the *CMV-mSmpd3* construct. We next examined the membrane localization of the WT and mutated nSMase2 proteins by indirect immunofluorescence and confocal microscopy using an antibody raised against the FLAG tag. Importantly, there was no alteration in the membrane localization pattern of mutant nSMase2 when compared with the WT protein (Fig. 2 E). These data confirm that the mutation of the predicted active site is the sole reason for the loss of catalytic activity of this enzyme in *fro/fro* mice.

### The *fro* mutation affects skeletal development

To investigate the effects of the *fro* mutation on the developing skeleton, we performed histological analysis of the long bones from embryonic day 15.5 (E15.5) *+/fro* and *fro/fro* embryos. There was an increased presence of unmineralized collagenous matrix in the cortical bones of the humerus (a representative long bone) of the *fro/fro* embryos in comparison to the cortical bones of their *+/fro* littermates (Fig. 3, A and B). This poor mineralization was not attributable to impaired osteoblast differentiation, as osterix (SP7) immunopositive cells were present in the cortical bones of the *fro/fro* mice (Fig. 3, C and D). Also, alkaline phosphatase activity was detected within the unmineralized matrix of the *fro/fro* bones, further indicating that osteoblast differentiation was not affected (Fig. 3, E and F). We next prepared total RNAs from the bones of newborn WT and *fro/fro* mice and examined the effects of the *fro* mutation on the expression of *Runx2* and *Atf4*, encoding two key transcription factors involved in early and late osteogenic differentiation, respectively. In agreement with our histological analysis of the embryonic mice, quantitative real-time PCR (qRT-PCR) analysis showed that the expression of these osteoblast marker genes were not altered in *fro/fro* bones (Fig. S1).

Although osteoblast differentiation was not affected in *fro/fro* mice, we did not observe any osterix-positive cells in the marrow space in the long bones of *fro/fro* embryos, whereas infiltration of osteoblast progenitors into the marrow space was normal in their *+/fro* littermates. Instead, we observed an unusual persistence of hypertrophic chondrocyte-like cells in the

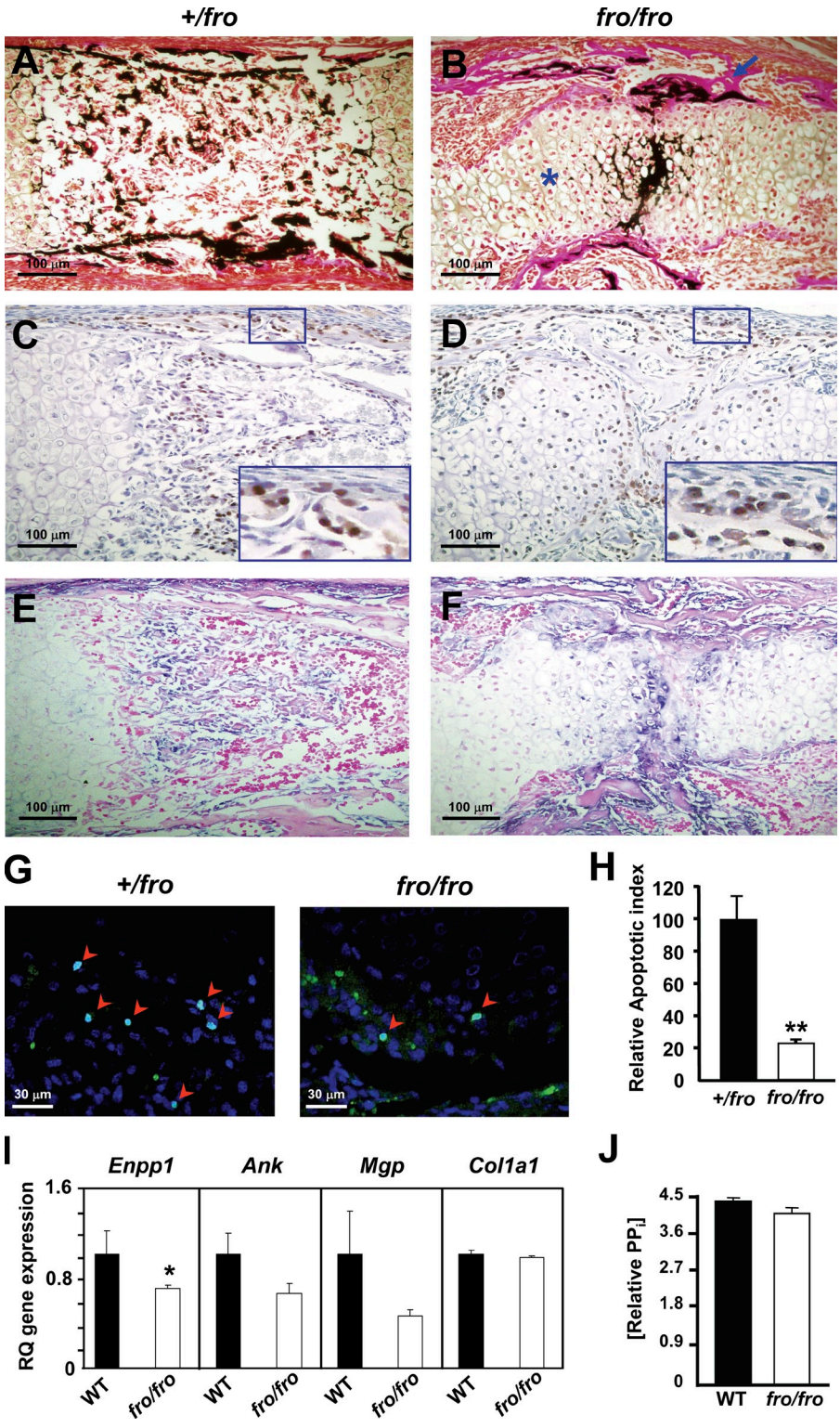


Figure 3. **Effects of *fro* mutation on the developing skeleton.** (A and B) Von Kossa and van Gieson staining of the humerus from E15.5 *+/fro* and *fro/fro* embryos. Note the unmineralized cortical bones (arrow) and the expanded hypertrophic zone (asterisk) in the *fro/fro* mice. (C and D) Immunostaining of humerus sections from E15.5 *+/fro* and *fro/fro* embryos using an antiosterix antibody shows osteoblast differentiation is unaffected in the latter genotype. For each panel, a magnified view of the marked area has been shown in the insets. (E and F) Incubation with a chromogenic substrate solution demonstrates the comparable presence of alkaline phosphatase activities in the *+/fro* and *fro/fro* bone sections. (G and H) TUNEL assay showing impaired apoptosis of hypertrophic chondrocytes in developing *fro/fro* endochondral bones ($n = 4$). Arrowheads indicate the TUNEL-positive cell nuclei. (I) qRT-PCR showing a mild down-regulation of *Enpp1* expression in the parietal bones from *fro/fro* mice. Note that there is no significant alteration of *Ank*, *Mgp*, and *Col1a1* expression in *fro/fro* bones. RQ, relative quantification. (J) $PP_i$ levels are comparable in both WT and *fro/fro* bone samples. Error bars represent standard deviations. *, $P < 0.05$; **, $P < 0.01$.

midshaft regions of the *fro/fro* long bones (Fig. 3, C and D). A possible explanation for this observation might be that the hypertrophic chondrocytes in these mutant bones were not undergoing apoptosis at a rate comparable with that of *+/fro* hypertrophic chondrocytes. To investigate this possibility, we performed TUNEL assay on the humerus sections from both *+/fro* and *fro/fro* embryos at E15.5. A decreased presence of TUNEL-positive nuclei in the *fro/fro* hypertrophic zones in comparison to the corresponding areas of the *+/fro* bones confirmed that there was indeed a reduction of the apoptosis of *fro/fro* hypertrophic chondrocytes (Fig. 3, G and H).

The presence of ALPL activity in the developing *fro/fro* bones suggests normal $PP_i$ hydrolysis in the ECM. However, the $PP_i$ levels in the ECM may increase because of an up-regulation of *Enpp1* and *Ank*, which encode two proteins critical for the maintenance of tissue homeostasis of this mineralization inhibitor

(Ho et al., 2000; Hessle et al., 2002). We analyzed the expression of these two genes by qRT-PCR and found that there was in fact a mild down-regulation of *Enpp1* expression in the bones of newborn *fro/fro* mice, whereas *Ank* expression was not altered (Fig. 3 I). Also, we did not observe any up-regulation of *Mgp* and *Col1a1* expression (Fig. 3 I). We then used a fluorogenic sensor to measure $PP_i$ levels in the bones of adult WT and *fro/fro* mice. We observed that $PP_i$ was present at comparable levels in the bone samples from both genotypes (Fig. 3 J). Collectively, these data suggest that the hypomineralization defect seen in *fro/fro* mice was not caused by the increase of MGP or $PP_i$ in the bone ECM.

### Loss of nSMase2 in osteoblasts affects mineralization in vitro

We next examined *Smpd3* expression in late-stage mouse embryos and also in tissues collected from WT mice at the preweaning age. The sense and antisense probes generated from the *Smpd3* cDNA were hybridized separately on fixed whole-embryo paraffin sections prepared from E16.5 WT embryos. The in situ hybridization analysis performed with the antisense probe showed a high level of *Smpd3* expression in all bone types, cartilage, and in the brain (Fig. 4 A). A similar *Smpd3* expression pattern was also observed in 2-wk-old mice (Fig. 4 B). Next, we examined *Smpd3* expression during the differentiation of MC3T3-E1 preosteoblasts cultured in the presence of ascorbic acid and β-glycerol phosphate. Under these culture conditions, we observed a progressive induction of *Smpd3* expression, which was down-regulated in fully mature osteoblasts (Fig. 4 C).

A high level of expression of *Smpd3* in embryonic and postnatal bones and in a differentiating osteoblastic cell line suggests a local role for this enzyme in bone. To examine whether nSMase2 deficiency in *fro/fro* bones causes a reduction of total nSMase activity, we prepared calvarial bone extracts from both *+/fro* and *fro/fro* mice and performed an in vitro enzymatic assay using $^{14}C$-labeled sphingomyelin (Marchesini et al., 2003). As a control experiment, we performed the same analysis on the extracts prepared from both *+/fro* and *fro/fro* brain tissues. As shown in Fig. 4 D, there was a comparable decrease of nSMase activities in both brain and bone extracts from *fro/fro* mice.

We next investigated whether a loss of nSMase2 activity affects the in vitro mineralization capacities of cultured osteoblasts. First, we transfected MC3T3-E1 preosteoblasts with siRNA oligonucleotides to knock down *Smpd3* gene expression. Gene expression analysis by qRT-PCR revealed that there was an ∼60% reduction of *Smpd3* expression in the siRNA-transfected cells (Fig. 4 E). We cultured both control and *Smpd3* siRNA-transfected cells in the presence of ascorbic acid and β-glycerol phosphate to induce differentiation and mineralization. Upon culturing for 10 d in the aforementioned medium, cells were stained with Alizarin red, a calcium-binding dye. We observed reduced mineralization in the cultures with *Smpd3* siRNA-transfected cells in comparison to the cultures with control siRNA-transfected cells (Fig. 4 F). This observation was further confirmed in experiments performed with primary osteoblasts isolated from the newborn *+/fro* and *fro/fro* mice. When cultured in the presence of ascorbic acid and β-glycerol phosphate, *fro/fro* osteoblast cultures showed reduced mineralization in comparison to the *+/fro* cultures (Fig. 4 G).

### Osteoblast-specific expression of *Smpd3* in *fro/fro* mice increases bone nSMase activity

Collectively, a decline of total nSMase activity in *fro/fro* bones and reduced in vitro mineralization by *fro/fro* osteoblasts (Fig. 4, D and G) strongly suggest a local and specific role for nSMase2 in bone. To investigate this in vivo, we overexpressed *Smpd3* specifically in the bones of *fro/fro* mice. For this purpose, we generated a *Col1a1-Smpd3* transgene construct using a 2.3-kb *Col1a1* promoter fragment, earlier shown to be specifically expressed in osteoblasts (Fig. 5 A). Pronuclear injection of this construct into fertilized mouse eggs resulted in four founders, of which two showed bone-specific expression of the transgene. No transgene expression was detected in any other tissue in these founders (Fig. 5 B). These founders were then mated with *+/fro* mice to first generate *+/fro;Col1a1-Smpd3* mice, which were mated again with *+/fro* mice to obtain *fro/fro;Col1a1-Smpd3* mice.

By visual examination, there was no gross skeletal abnormalities in the *fro/fro;Col1a1-Smpd3* mice. Also, these mice survived the perinatal death routinely seen in *fro/fro* mice (described in Fig. 6). In agreement with our transgene expression data, we observed a threefold increase of total nSMase activities in the bones of newborn *fro/fro;Col1a1-Smpd3* mice in comparison to the bones of *fro/fro* mice, whereas brain nSMase activities remained indistinguishable between these two genotypes (Fig. 5 C). Interestingly, despite a significant increase of bone nSMase activities in *fro/fro;Col1a1-Smpd3* mice, there was no detectable decrease of total bone sphingomyelin levels (Fig. 5 D). However, an increase of total ceramide levels in the bones of *fro/fro;Col1a1-Smpd3* mice was observed when compared with the *fro/fro* bones (Fig. 5 E). Interestingly, we found a significant increase of several long-chain ceramide species (e.g., C16, C24, and C24:1) in the bones of the former genotype (Fig. 5 F). No significant alterations were observed in total dihydroceramide levels in the bone extracts prepared from any of the mouse models analyzed (Fig. 5 G). Also, several known serum parameters affecting ECM mineralization (e.g., calcium, $P_i$, and alkaline phosphatase levels) were unaltered in the *fro/fro;Col1a1-Smpd3* mice (Fig. 5, H–J).

Finally, we compared the expression of *Enpp1*, *Ank*, *Mgp*, and *Col1a1* by qRT-PCR in the parietal bones of newborn *fro/fro* and *fro/fro;Col1a1-Smpd3* mice. We observed significant up-regulation of *Enpp1* and *Ank*, but not *Mgp*, expression. *Col1a1* gene expression was mildly up-regulated in *fro/fro;Col1a1-Smpd3* bones in comparison with *fro/fro* bones (Fig. S2).

### Normal bone mineralization in *fro/fro;Col1a1-Smpd3* mice

We next examined the skeletal phenotype in *fro/fro;Col1a1-Smpd3* mice. Micro-CT analysis of the humerus from 15.5-d-old *fro/fro* embryos showed poorly mineralized cortical bones, which were fully mineralized in the *fro/fro;Col1a1-Smpd3*

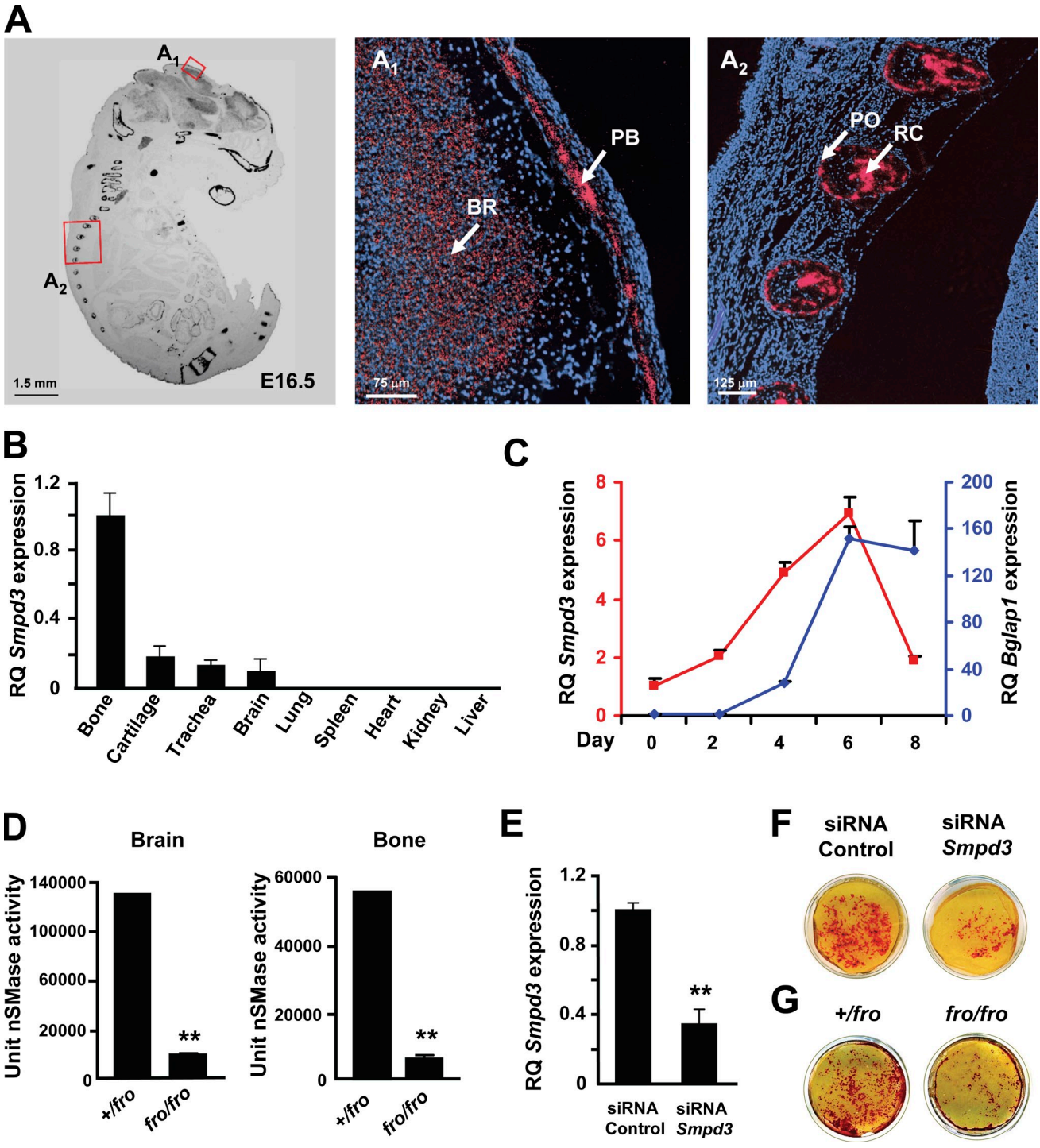


Figure 4. ***Smpd3* expression and function in osteoblasts.** (A) In situ hybridization showing *Smpd3* expression in different skeletal elements in an E16.5 WT mouse embryo. The magnified views of the areas in red boxes are shown in $A_1$ and $A_2$ (PB, parietal bone of the skull cap; BR, brain; PO, periosteum in the rib; and RC, rib cartilage). Red stain represents the localization of the *Smpd3* transcript, whereas the blue stain represents the nucleus. (B) qRT-PCR showing high levels of *Smpd3* expression in bone, brain, and cartilage. Tissues were collected from a 2-wk-old WT mouse. All expression analyses were performed using *hypoxanthine guanine phosphoribosyl transferase* (*Hprt*) expression in the tissue as an internal control and *Smpd3* expression in the bone as a calibrator (RQ, relative quantification). (C) *Smpd3* and *Bglap1* (red and blue lines, respectively) gene expression analysis in differentiating MC3T3-E1 preosteoblasts at five different time points. *Smpd3* expression reaches its peak by day 6. Late osteoblast marker *Bglap1* expression was used to monitor terminal differentiation of the MC3T3-E1 cells. (D) A mixed micelle assay using $^{14}$C-labled methyl-sphingomyelin shows a significant decrease in nSMase activity in both brain and bone tissues collected from the *fro/fro* mice. (E) *Smpd3* knockdown by using an siRNA technique in MC3T3-E1 preosteoblasts. (F) Alizarin red staining shows reduced in vitro mineral deposition in cultures of MC3T3-E1 cells transfected by *Smpd3* siRNAs in comparison with the control group. (G) Alizarin red staining shows reduced mineral deposition in cultures of differentiated *fro/fro* osteoblasts in comparison with the *+/fro* osteoblasts. The cultures were grown for 10 d in an osteogenic medium containing ascorbic acid and β-glycerol phosphate. Error bars represent standard deviations. **, $P < 0.01$.

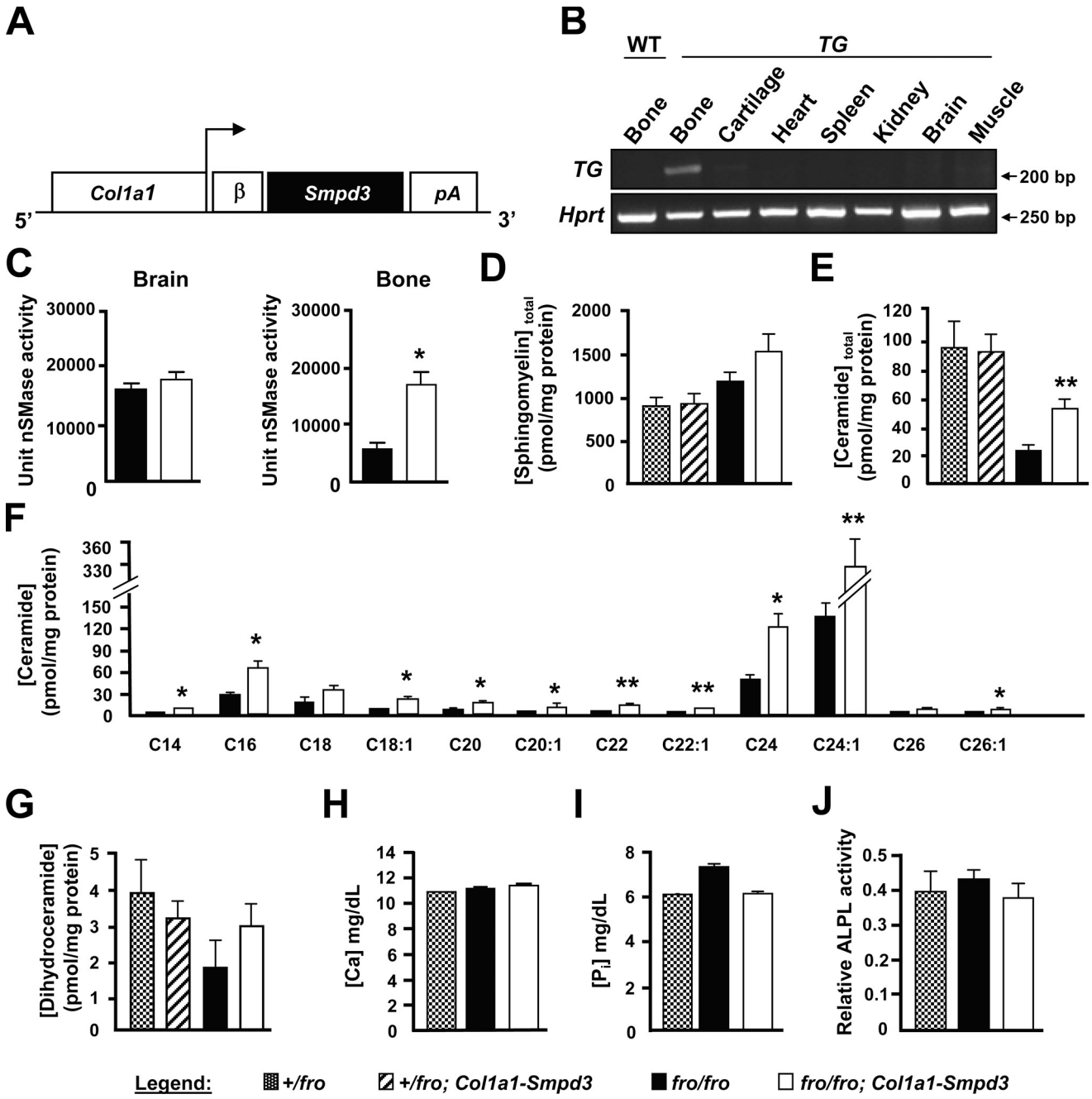


Figure 5. **Biochemical analysis of tissue and serum samples from *fro/fro;Col1a1-Smpd3* mice.** (A) Schematic representation of the *Col1a1-Smpd3* transgene construct. (B, top) Semiquantitative PCR analysis confirming bone-specific expression of the transgene (*TG*). (bottom) *Hprt* expression analysis has been shown as a control for the cDNA amount. Amplicon sizes in base pairs are indicated on the left. (C) Enzymatic assays using $^{14}$C-labled methyl-sphingomyelin shows no change in nSMase activity in *fro/fro;Col1a1-Smpd3* brain samples. As expected, in *fro/fro;Col1a1-Smpd3* bone samples, the nSMase activity is increased in comparison with the *fro/fro* bone samples. (D–G) Lipid analysis using liquid chromatography/mass spectrometry of sphingomyelin (D), total ceramide (E), individual ceramide species (F), and dihydroceramide (G). A significant increase of total ceramide levels is caused by the increase of several long-chain ceramide species in *fro/fro* bones ($n = 4$). (H–J) Serum calcium (H), $P_i$ (I), and alkaline phosphatase (J) activities are comparable in *+/fro*, *fro/fro*, and *fro/fro;Col1a1-Smpd3* mice ($n = 5$). Error bars represent standard deviations. *, $P < 0.05$; **, $P < 0.01$.

embryos at the same developmental stage. Interestingly, a reduced presence of mineral in the marrow compartment of both *fro/fro* and *fro/fro;Col1a1-Smpd3* long bones was noted, indicating that the chondrocyte phenotype was largely unaffected in the latter genotype (Fig. 6 A). The aforementioned observation was further confirmed by Alcian blue staining of the humeri sections from WT, *fro/fro*, and *fro/fro;Col1a1-Smpd3* mice. We observed that, as was the case in the long bones from the *fro/fro* mice, the marrow compartment in the long bones of *fro/fro;Col1a1-Smpd3* mice was full of densely packed chondrocytes within a cartilage matrix (Fig. 6 B). We next examined the skeleton of newborn *fro/fro;Col1a1-Smpd3* mice. Osteoblast-specific expression of *Smpd3* completely corrected the *fro/fro* skeletal abnormalities (Fig. 6 C). X-ray analysis showed that there

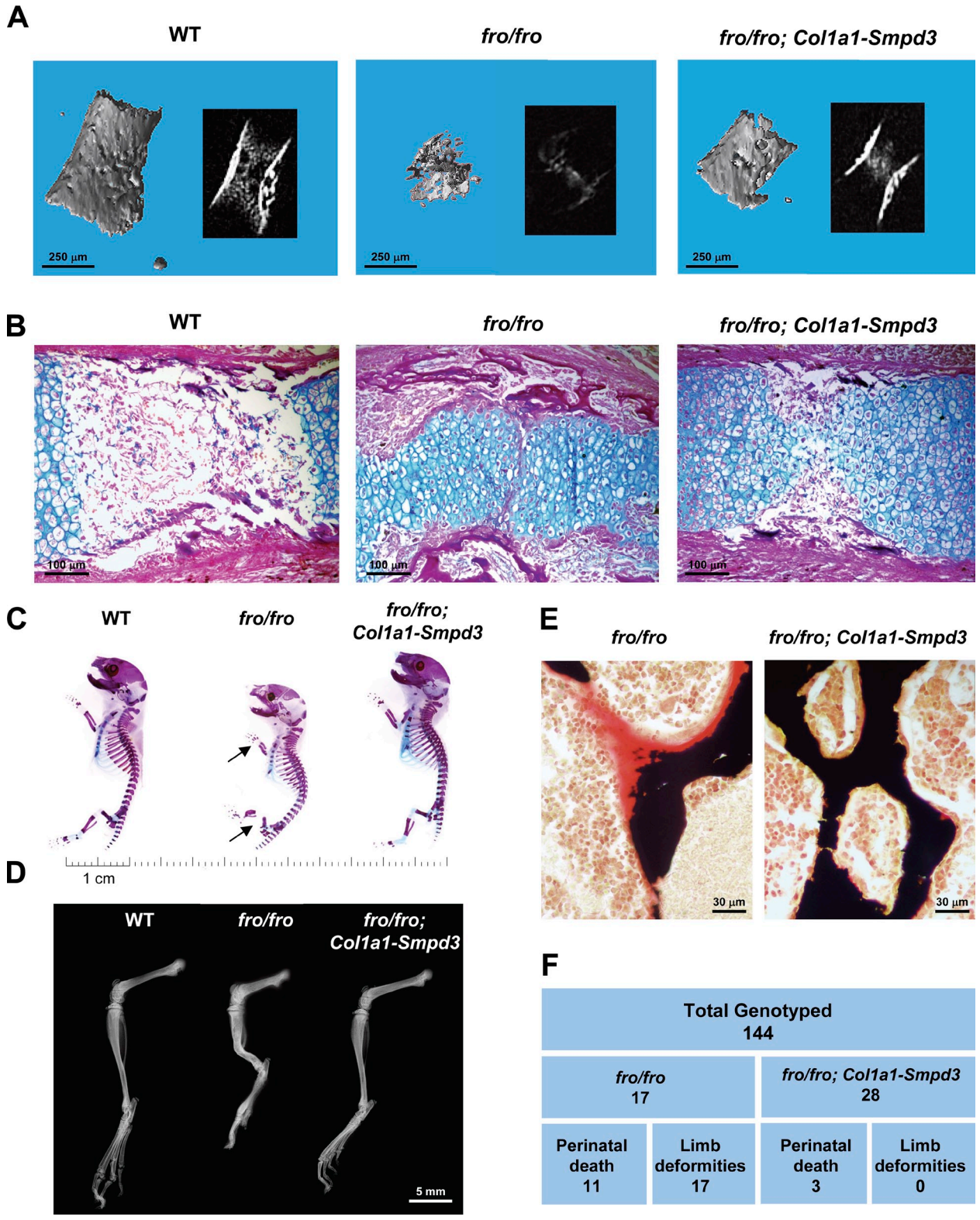


Figure 6. **Analysis of *fro/fro;Col1a1-Smpd3* bones.** (A) Micro-CT analysis of E15.5 *fro/fro* humerus showing a poorly mineralized bone collar and cartilage matrix. Although bone collar mineralization defects are completely rescued in *fro/fro;Col1a1-Smpd3* embryos, mineralization defects in the cartilage matrix are still present. Insets show the cross-sectional x-ray images of the analyzed bones. (B) Alcian blue and van Gieson staining of humerus sections from E15.5 *fro/fro* embryos confirm the micro-CT findings. Note the abnormal presence of the hypertrophic chondrocyte-like cells in the shaft region of the *fro/fro* humerus. This latter phenotype is largely unaffected in the *fro/fro;Col1a1-Smpd3* long bones. (C) Skeletal preparations indicate a full rescue of the *fro/fro* bone deformities (arrows) in the newborn *fro/fro;Col1a1-Smpd3* mice. (D) Radiographical analysis shows that the limb abnormalities are absent in 1-mo-old *fro/fro;Col1a1-Smpd3* mice. (E) Von Kossa and van Gieson staining of vertebral bone sections from 1-mo-old *fro/fro* and *fro/fro;Col1a1-Smpd3* littermates demonstrate a complete rescue of the mineralization defects in the latter genotype. (F) Table showing genotyping data. Skeletal abnormalities were not seen in any of the *fro/fro;Col1a1-Smpd3* mice analyzed.

was no recurrence of the skeletal abnormalities in the adult *fro/fro;Col1a1-Smpd3* mice (Fig. 6 D). Also, we observed an absence of abnormally high osteoid volume in the bones of this latter model (Fig. 6 E).

We analyzed a total of 144 mice from the aforementioned breeding experiments, of which 17 were *fro/fro*. All of these mice had limb deformities, and 11 of them died perinatally. On the other hand, out of a total of 28 *fro/fro;Col1a1-Smpd3* mice generated through this breeding, only three died perinatally, whereas none of them showed any kind of skeletal abnormalities (Fig. 6 F). We tested the significance of these data using the standard Pearson's $\chi^2$ test and found that for the rescue of both skeletal phenotype and perinatal death, the p-values were far below the commonly accepted 5% threshold for significance.

## Discussion

Analysis of novel, genetically modified mouse models with skeletal and dental mineralization defects may provide critical information on as yet unidentified regulators of ECM mineralization and, thereby, improve our understanding of this important physiological process. Recently, a loss-of-function mutation in the *Smpd3* gene has been identified in a mouse model (*fro/fro*), which shows severe bone and tooth mineralization defects (Guenet et al., 1981; Aubin et al., 2005). The *fro/fro* skeletal abnormalities are similar to the skeletal pathology seen in patients with certain forms of osteogenesis imperfecta that do not involve any mutation in collagen genes (Glorieux et al., 2002). As is the case with these patients, the most common parameters affecting ECM mineralization, e.g., serum calcium, $P_i$, and alkaline phosphatase levels, are not decreased in *fro/fro* mice. Furthermore, when analyzed by histology, the unmineralized bone matrix appears to be secreted normally in these mice. Collectively, these observations suggest that *Smpd3* might affect ECM mineralization through a novel mechanism.

In an earlier study, the skeletal phenotype of *Smpd3*$^{-/-}$ mice has been described as a form of chondrodysplasia (Stoffel et al., 2005). In agreement with this finding, we observed a significantly impaired apoptosis of hypertrophic chondrocytes, possibly caused by reduced ceramide levels during early skeletal development in *fro/fro* embryos. Additionally, we also observed poor mineralization of the matrix secreted by osteoblasts that severely affects the strength of the cortical bones in these embryos. This novel finding explains the long bone deformities in *fro/fro* mice.

Our data suggest that hypomineralization of bone ECM in *fro/fro* mice is not caused by the elevated levels of mineralization inhibitors MGP or $PP_i$ (Fig. 3, I and J). We observed a mild down-regulation of *Enpp1* in *fro/fro* bones, whereas both *Ank* and *Enpp1* expressions were significantly up-regulated in the bones of *fro/fro;Col1a1-Smpd3* mice. Interestingly, up-regulation of these two genes in the latter model did not prevent the rescue of the bone mineralization defects. These data suggest that there might be a compensatory interplay between the positive (nSMase2) and negative (ANK and ENPP1) regulators of bone ECM mineralization.

Our current study establishes an osteoblast-specific role of *Smpd3* in bone mineralization and several lines of evidence suggest that the *Smpd3*-encoded enzyme nSMase2 acts as a local modulator of ECM mineralization in bone. First, *Smpd3* is highly expressed in bone, and its expression progressively increases as osteoblasts mature. Second, loss of *Smpd3* expression in both siRNA-treated MC3T3-E1 preosteoblasts and in *fro/fro* primary osteoblasts causes impaired mineral deposition in cultures. Finally, osteoblast-specific expression of *Smpd3* in *fro/fro* bones completely rescues the skeletal abnormalities. Collectively, all these findings provide unambiguous demonstration of a direct osteoblast/mineralization effect for the locally synthesized nSMase2 in osteoblasts. Furthermore, a normal skeletal appearance in *fro/fro;Col1a1-Smpd3* mice suggests that the loss of nSMase2 activity in osteoblasts is the major cause of the *fro/fro* phenotype.

At this point, we cannot fully rule out an indirect systemic effect of nSMase2 enzymatic activity from other tissues on the developing skeleton. However, in view of our findings that osteoblast-specific expression of *Smpd3* in *fro/fro* mice corrects the bone but not the cartilage phenotype, we do not consider this as a likely possibility. This latter finding also suggests a tissue-specific role for nSMase2 in the developing skeleton with apparent independent roles in bone and cartilage.

Both *fro/fro* and the gene-targeted *Smpd3*$^{-/-}$ mice share similar gross skeletal abnormalities, i.e., short-limbed dwarfism, deformation of long bones, abnormally formed rib cages, and abnormalities in growth plate cartilage. However, Stoffel et al. (2005, 2007), in their gene-targeted model, did not observe bone and tooth mineralization abnormalities, which are seen in all *fro/fro* mice. This apparent discrepancy can be explained by differences in the analytical methods used to characterize the two mouse lines. Stoffel et al. (2005, 2007) analyzed the mineralization status of the *Smpd3*$^{-/-}$ mice solely by bone mineral density analysis, which determines the total bone mineral content and is not suitable for detecting an increase in unmineralized bone matrix. In contrast, we analyzed the *fro/fro* bones using a histomorphometric technique on undecalcified samples, commonly used to detect skeletal mineralization defects.

Although Stoffel et al. (2005, 2007) suggested that the phenotypic variations in *fro/fro* and *Smpd3*$^{-/-}$ mice can be attributable to the presence of any additional genetic alterations in the former strain, such mutations would have been fully segregated during the propagation of *fro/fro* mice in multiple laboratories over the last two decades. This inference, together with the observation that the fully penetrant *fro/fro* phenotype, including the severe hypomineralization defect, is always associated with the *Smpd3* deletion mutation reported by Aubin et al. (2005), clearly identifies the loss of nSMase2 function as the sole cause of the *fro/fro* phenotype. Indeed, our current data showing a complete rescue of the skeletal phenotypes in *fro/fro;Col1a1-Smpd3* mice expressing *Smpd3* in osteoblasts rules out the possibility of the presence of any additional mutation in *fro/fro* mice that may cause the observed mineralization defects.

Our results demonstrate an intrinsic loss of nSMase activity attributable to the *fro* mutation. The translocation of nSMase2 from the Golgi compartment to the plasma membrane

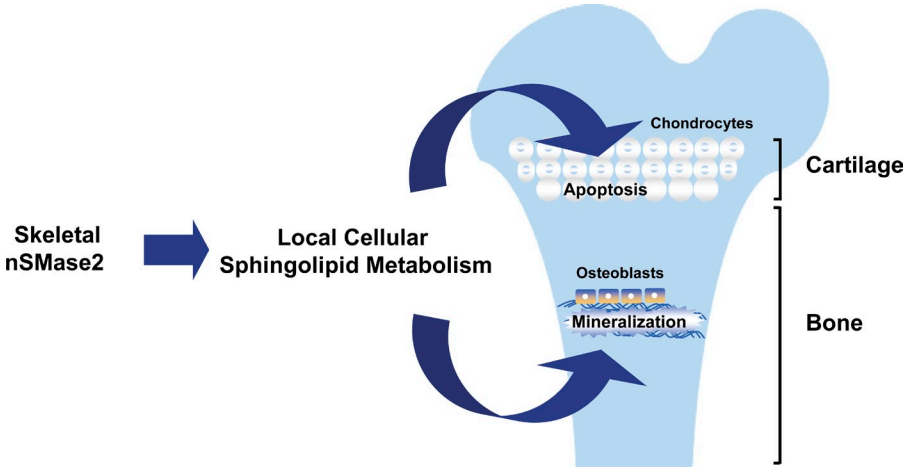


Figure 7. **A model depicting the local activities of nSMase2 in skeletal tissues.** The cell-autonomous activity of nSMase2 in bone promotes ECM mineralization. In the cartilage, nSMase2 enzymatic activity is necessary for the normal apoptosis of hypertrophic chondrocytes.

and its recycling back to the Golgi is a highly dynamic and regulated process. Notably, preventing nSMase2 recycling has been shown to increase nSMase activity and ceramide levels, suggesting adverse physiological consequences for alterations in localization of this enzyme (Milhas et al., 2010). Considering the critical nature of this process, we examined whether the reduced nSMase activities in *fro/fro* tissues are attributable to an impaired nSMase2 localization or are caused by the loss of its catalytic activity. Our cell culture data confirm that the mutant nSMase2 localizes identically to WT nSMase2 and indicate that the reduced tissue nSMase activity in *fro/fro* mice is likely to be caused by the disruption of the enzyme's catalytic site.

nSMase2 cleaves sphingomyelin to generate the lipid second messenger ceramide (Merrill et al., 1997; Wu et al., 2010). Thus, a loss of functional nSMase2 could have dual effects, i.e., both a decrease in ceramide levels and an increase in sphingomyelin levels in tissues in which *Smpd3* is normally expressed. Indeed, a recent study suggested a crucial role for sphingomyelin and its degradation in bone and dentin mineralization (Goldberg et al., 2008). However, as sphingomyelin, being an integral component of all cell membranes, is present in all tissues in relatively high amounts and because only a small fraction of it is cleaved by the nSMase2 enzymatic activity, a loss-of-function mutation in *Smpd3* as such may not have any significant effects on the total tissue sphingomyelin levels. Indeed, we did not observe any difference in total sphingomyelin levels between *+/fro* and *fro/fro* bones. This observation suggests that increased sphingomyelin levels in bone attributable to the loss of nSMase2 activity may not account for the ECM mineralization defects in *fro/fro* mice. Although we could not detect any significant alteration in tissue sphingomyelin levels, we found a remarkable decrease of various ceramide species, particularly those with long chains, in *fro/fro* bones in comparison to the control *+/fro* bones. Currently, it is not clear how ceramide might affect bone ECM mineralization. Ceramide acting as a second messenger can affect several signaling pathways and may alter as yet unknown downstream regulators critical for bone ECM mineralization.

In conclusion, the *fro/fro* mice lacking a functional nSMase2 provide a unique opportunity to investigate a novel mechanism involved in vertebrate hard tissue mineralization. The data we present here suggest that a local nSMase2 function is required for a normal bone mineralization and for the normal apoptosis of hypertrophic chondrocytes in the cartilage during early skeletal development (Fig. 7). Collectively, these data demonstrate, for the first time, the tissue-specific roles for this enzyme in the developing skeleton. Further analyses of the mouse models reported here may reveal the molecular mechanisms underlying the pathophysiology of certain forms of osteomalacia and osteogenesis imperfecta in humans.

## Materials and methods

### DNA constructs

The DNA construct for osteoblast-specific expression of the *Smpd3* transgene was generated using a 2.3-kb *Col1a1* promoter fragment (Rossert et al., 1995). A full-length *Smpd3* cDNA (American Type Culture Collection) preceded by a rabbit β-globin intron was inserted in between the *Col1a1* promoter fragment and a SV40 polyadenylation signal. The transgene sequence was released from the plasmid backbone by SacII restriction digestion and was used for pronuclear injection. A PCR-based technique was used to introduce the *fro* mutation into the WT cDNA. Both WT and mutant (*fro*) *Smpd3* cDNAs were cloned in pIRES-hrGFP-1α (Agilent Technologies).

### Mice

Generation of *fro/fro* mice was described previously (Aubin et al., 2005). Transgenic founders were generated by pronuclear injections at the McIntyre Cancer Center Transgenic Core Facility at McGill University following standard techniques. All mice were maintained in a pathogen-free standard animal facility, and the experimental procedures were performed following an animal use protocol approved by the Animal Care Committee of McGill University. Genotypes were determined by PCR on genomic DNAs isolated from the tail biopsies. The following primers were used for the genotyping of the *fro* mutation: 5′-GGGACGACGTCTGCCTCAGG-3′, 5′-TTAGAGGTCCCAACCACAGG-3′, and 5′-CCCAGGTGCTGGGCAGAAGG-3′. With these three primers, it is possible to amplify specific WT (145 bp) and mutant (189 bp) DNA fragments. The *Col1a1-Smpd3* transgene integration was detected using the following primer pair specific for the SV40 polyadenylation signal: 5′-CAGCTCTCCATCAAGATGGT-3′ and 5′-CCGGTTTGGACTCAGAGTAT-3′.

### Gene expression analysis

Gene expression analyses were performed using a qRT-PCR system (model 7500; Applied Biosystems). Total RNA was extracted from different tissues with TRIZOL reagent (Invitrogen) and subjected to DNase I (Invitrogen) treatment. The first-strand cDNA synthesis and qRT-PCR were performed using a high-capacity cDNA reverse transcription kit (Applied Biosystems) and SYBR green quantitative PCR master mix (Maxima; Fermentas), respectively. The following primer pairs were used: 5′-AGAAACCCGGTCCTCGTACT-3′ and 5′-CCTGACCAGTGCCATTCTTT-3′ for *Smpd3* expression

and 5′-AAGCAGGAGGGCAATAAGGT-3′ and 5′-CAAGCAGGGTTAAGCTCACA-3′ for *Bglap1* expression. For in situ hybridization analyses, embryos were fixed in 4% PFA, embedded in paraffin, and sectioned at 5-µm thickness. A full-length *Smpd3* cDNA was used to generate $^{35}$S-labeled sense and antisense riboprobes.

**Skeletal preparation and histological analysis**

Skeletal tissues from newborn and adult mice were fixed overnight in 95% ethanol, stained in 0.015% Alcian blue dye (Sigma-Aldrich) in a 1:4 solution of glacial acetic acid and absolute ethanol for 24 h, and treated with 2% potassium hydroxide until the soft tissues were dissolved. The mineralized tissues were stained by 0.005% Alizarin red (Sigma-Aldrich) solution in 1% potassium hydroxide and clarified in 1% potassium hydroxide/20% glycerol for ≥2 d. For plastic sectioning, vertebrae were fixed overnight in 4% PFA/PBS, embedded in methyl methacrylate, and sectioned (7-µm thickness), and von Kossa and van Gieson staining was applied. Unmineralized bone sections were analyzed using Osteomeasure software (Osteometrics, Inc.). Mouse embryos were fixed in 4% PFA/PBS, pH 7.4, overnight and embedded in paraffin. 5-µm-thick sections were submitted to von Kossa, Alcian blue, and van Gieson staining. Images were taken at room temperature using a light microscope (DM200; Leica) with a 20× (numerical aperture of 0.40) or 40× (numerical aperture of 0.65) objective. All histological images were captured using a camera (DP72; Olympus), acquired with DP2-BSW software (XV3.0; Olympus), and processed using Photoshop (Adobe). The TUNEL assay was performed on E15.5 embryos to evaluate in vivo chondrocyte apoptosis as per the manufacturer's instructions (Deadend Fluorometric TUNEL System kit; Promega).

**Immunofluorescence and confocal microscopy**

MCF-7 cells (15 × $10^4$/dish) were seeded in 35-mm confocal dishes (MatTek), and after 24 h, cells were transiently transfected with 1 µg *Smpd3* or *mSmpd3* cloned in the pIRES-hrGFP-1α expression vector. After 24 h, cells were fixed with 3.7% PFA for 10 min, permeabilized with 100% methanol for 5 min at −20°C, and blocked with 2% human serum in PBS for 30 min at room temperature. Cells were probed with or without anti-FLAG (1:1,000; Sigma-Aldrich) antibody in 2% serum for 2 h at room temperature, washed with 3× PBS, and probed with fluorescent secondary antibody (1:200 anti–mouse Alexa Fluor *555*; 30–45 min at room temperature). After washing with 3× PBS, nuclei were visualized with DRAQ5 staining (1:500 in PBS). Images were captured with a confocal microscope (LSM 510 Meta; Carl Zeiss).

**Immunoblotting**

Protein samples were separated on 4–20% gradient Tris-HCl gels (Bio-Rad Laboratories) at a constant current of 40 mA before transfer to nitrocellulose membrane in Tris/glycine buffer (100 V for 30 min at 4°C). Membranes were blocked (5% milk in 0.1% Tween in PBS for 30 min) and incubated overnight at 4°C with anti-FLAG (Sigma-Aldrich), anti-nSMase2 (Santa Cruz Biotechnology, Inc.), or antiactin (Sigma-Aldrich) primary antibodies at a 1:1,000, 1:500, or 1:20,000 dilution, respectively. Membranes were washed (3× in 0.1% Tween in PBS), probed with HRP-conjugated mouse or rabbit secondary antibody (1:5,000 in 5% milk in 0.1% Tween in PBS) for 30–45 min at room temperature, and washed (3× in 0.1% Tween in TBS). Proteins were visualized by enhanced chemiluminescence (Thermo Fisher Scientific).

**Transient transfection with siRNAs, cell culture, and in vitro mineralization**

MC3T3-E1 cells were transfected with 50 ng/µl of *Smpd3* (SI01426999; QIAGEN) or control (1027284; QIAGEN) annealed double-stranded siRNAs and cultured in α-MEM (Invitrogen) supplemented with 10% FBS (PAA Laboratories) and 100 U/ml penicillin-streptomycin at 37°C under 5% $CO_2$ in a humidified incubator. Primary osteoblast isolation from calvaria, in vitro differentiation and culture, and Alizarin red staining for mineral deposition were performed as described previously (Li et al., 2011).

**Radiography and micro-CT analysis**

Radiography and micro-CT analyses of the skeletal samples were performed at the Centre for Bone and Periodontal Research Core Facility at McGill University using an x-ray imaging system (XPERT; Kubtec) and micro-CT system (SkyScan), respectively. For micro-CT analyses, the x-ray source was operated at 45 kV and at 222 µA (maximum power). Images were captured using a 12-bit, cooled charge-coupled device camera (1,024 by 1,024 pixels) coupled by a fiber optics taper to the scintillator. Samples were scanned at a magnification resulting in a pixel size of 4.79 µm. Using a rotation step of 0.9° and an exposition time of 2,240 ms for each step, images were generated, giving a scanning time of 30 min. The cross sections along the specimen long axis were reconstructed using NRecon software (SkyScan), with a distance between each cross section of 9.58 µm. Each cross section was reduced in half-size to facilitate the analysis, giving of a voxel of 9.58 × 9.58 × 9.58 $\mu m^3$. CT-Analyser and 3D Creator software (both from SkyScan) were used to analyze and to perform 3D rendering, respectively.

**Serum biochemistry**

Serum calcium and $P_i$ levels were measured using commercially available kits (Diagnostic Chemicals Limited). Serum ALPL levels were measured as described previously (Li et al., 2011), whereas tissue $PP_i$ levels were measured using a fluorogenic sensor following the manufacturer's instructions (Advancing Assay Technologies Bioquest, Inc.).

**Sphingomyelinase assays and lipid measurements**

Limbs and skullcaps were snap frozen in liquid nitrogen and crushed before further homogenization in 20 mM Tris buffer containing protease inhibitors using an autohomogenizer. Brain tissue was homogenized directly in the same buffer. Aliquots of homogenate were removed for the estimation of protein concentration by the Bradford assay. In vitro analysis of nSMase activity was performed using a mixed micelle assay as described previously (Marchesini et al., 2003). In brief, duplicate aliquots (20–30 µg protein) of homogenate were diluted to 100 µl in neutral buffer containing 25 mM Tris, pH 7.4, 5 mM EDTA, 0.2% Triton X-100, and protease inhibitors. The reaction was started by adding 100 µl assay buffer containing 200 µM sphingomyelin, 100 µM phosphatidylserine, and 100,000 cpm $^{14}$C-labeled methyl-sphingomyelin reconstituted in 25 mM Tris, pH 7.4, 10 mM $MgCl_2$, 5 mM DTT, and 0.2% Triton X-100. After incubation for 30 min at 37°C, reactions were stopped by the addition of 1.5 ml chloroform/methanol (2:1). 400 µl of water was added, and samples were vortexed and spun at 3,000 rpm for 5 min at room temperature. Next, 800 µl of the upper phase was added to 4 ml scintillation fluid, vortexed, and counted. 10 µl assay buffer, representing 2 nmol sphingomyelin, was also counted to allow conversion of results from counts per minute to picomoles of ceramide per milligram of protein per hour. For lipid analysis by mass spectrometry, after homogenization, lysate containing 200 µg–1 mg protein was analyzed for sphingomyelin, ceramide, and dihydroceramide levels by tandem liquid chromatography/mass spectrometry as previously described (Bielawski et al., 2010). Lipid levels were normalized to cellular protein.

**Data analysis**

All results are shown as means ± the standard deviation. Statistical analyses were performed by Student's *t* test, with $P < 0.05$ considered significant as indicated by a single asterisk (**, $P < 0.01$). Standard Pearson's $\chi^2$ test was used to test the significance of the rescue of both skeletal phenotype and perinatal death.

**Online supplemental material**

Fig. S1 shows qRT-PCR analysis of *Runx2* and *Atf4* expression in newborn *fro/fro* bones. Fig. S2 shows qRT-PCR analysis of *Enpp1*, *Ank*, *Mgp*, and *Col1a1* expression in the bones from newborn *fro/fro* and *fro/fro;Col1a1-Smpd3* mice. Fig. S3 shows qRT-PCR analysis of *Runx2*, *Col1a1*, *Atf4*, and *Bglap1* expression in the control and Smpd3 siRNA-treated MC3T3-E1 cells and *Runx2*, *Atf4*, *Bglap1*, and *Smpd3* expression in WT and *+/fro* mice. Online supplemental material is available at http://www.jcb.org/cgi/content/full/jcb.201102051/DC1.

We thank Drs. Geoffrey Hendy and Houman Homayoun for critical reading of the manuscript.

This work was supported by operating grant 216548 from the Canadian Institutes of Health Research and a seed grant from the Osteogenesis Imperfecta Foundation to M. Murshed. Z. Khavandgar receives a stipend from the McGill University Health Centre Research Institute, and M. Murshed receives salary support from the Fonds de la Recherche en Santé du Québec grant 16302. Additional support for this work was provided by National Institutes of Health grant GM43825 to Y.A. Hannun. M. Murshed and M.D. McKee are members of the Centre for Bone and Periodontal Research, and additional support is gratefully acknowledged from the Fonds de la Recherche en Santé du Québec Réseau de Recherche en Santé Buccodentaire et Osseuse.

Submitted: 9 February 2011
Accepted: 23 June 2011

## References


Aubin, I., C.P. Adams, S. Opsahl, D. Septier, C.E. Bishop, N. Auge, R. Salvayre, A. Negre-Salvayre, M. Goldberg, J.L. Guénet, and C. Poirier. 2005. A deletion in the gene encoding sphingomyelin phosphodiesterase 3 (Smpd3) results in osteogenesis and dentinogenesis imperfecta in the mouse. *Nat. Genet.* 37:803–805. doi:10.1038/ng1603

Bielawski, J., J.S. Pierce, J. Snider, B. Rembiesa, Z.M. Szulc, and A. Bielawska. 2010. Sphingolipid analysis by high performance liquid chromatography-tandem mass spectrometry (HPLC-MS/MS). *Adv. Exp. Med. Biol.* 688: 46–59. doi:10.1007/978-1-4419-6741-1_3

Bose, R., M. Verheij, A. Haimovitz-Friedman, K. Scotto, Z. Fuks, and R. Kolesnick. 1995. Ceramide synthase mediates daunorubicin-induced apoptosis: an alternative mechanism for generating death signals. *Cell*. 82:405–414. doi:10.1016/0092-8674(95)90429-8

Fleisch, H., and S. Bisaz. 1962. Mechanism of calcification: inhibitory role of pyrophosphate. *Nature*. 195:911. doi:10.1038/195911a0

Glorieux, F.H., L.M. Ward, F. Rauch, L. Lalic, P.J. Roughley, and R. Travers. 2002. Osteogenesis imperfecta type VI: a form of brittle bone disease with a mineralization defect. *J. Bone Miner. Res.* 17:30–38. doi:10.1359/jbmr.2002.17.1.30

Goldberg, M., S. Opsahl, I. Aubin, D. Septier, C. Chaussain-Miller, A. Boskey, and J.L. Guenet. 2008. Sphingomyelin degradation is a key factor in dentin and bone mineralization: lessons from the fro/fro mouse. The chemistry and histochemistry of dentin lipids. *J. Dent. Res.* 87:9–13. doi:10.1177/154405910808700103

Guenet, J.L., R. Stanescu, P. Maroteaux, and V. Stanescu. 1981. Fragilitas ossium: a new autosomal recessive mutation in the mouse. *J. Hered.* 72:440–441.

Hessle, L., K.A. Johnson, H.C. Anderson, S. Narisawa, A. Sali, J.W. Goding, R. Terkeltaub, and J.L. Millan. 2002. Tissue-nonspecific alkaline phosphatase and plasma cell membrane glycoprotein-1 are central antagonistic regulators of bone mineralization. *Proc. Natl. Acad. Sci. USA*. 99:9445–9449. doi:10.1073/pnas.142063399

Ho, A.M., M.D. Johnson, and D.M. Kingsley. 2000. Role of the mouse ank gene in control of tissue calcification and arthritis. *Science*. 289:265–270. doi:10.1126/science.289.5477.265

Kolak, M., J. Westerbacka, V.R. Velagapudi, D. Wågsäter, L. Yetukuri, J. Makkonen, A. Rissanen, A.M. Häkkinen, M. Lindell, R. Bergholm, et al. 2007. Adipose tissue inflammation and increased ceramide content characterize subjects with high liver fat content independent of obesity. *Diabetes*. 56:1960–1968. doi:10.2337/db07-0111

Li, J., Z. Khavandgar, S.H. Lin, and M. Murshed. 2011. Lithium chloride attenuates BMP-2 signaling and inhibits osteogenic differentiation through a novel WNT/GSK3- independent mechanism. *Bone*. 48:321–331. doi:10.1016/j.bone.2010.09.033

Luo, G., P. Ducy, M.D. McKee, G.J. Pinero, E. Loyer, R.R. Behringer, and G. Karsenty. 1997. Spontaneous calcification of arteries and cartilage in mice lacking matrix GLA protein. *Nature*. 386:78–81. doi:10.1038/386078a0

Marchesini, N., C. Luberto, and Y.A. Hannun. 2003. Biochemical properties of mammalian neutral sphingomyelinase 2 and its role in sphingolipid metabolism. *J. Biol. Chem.* 278:13775–13783. doi:10.1074/jbc.M212262200

Merrill, A.H. Jr., E.M. Schmelz, D.L. Dillehay, S. Spiegel, J.A. Shayman, J.J. Schroeder, R.T. Riley, K.A. Voss, and E. Wang. 1997. Sphingolipids—the enigmatic lipid class: biochemistry, physiology, and pathophysiology. *Toxicol. Appl. Pharmacol.* 142:208–225. doi:10.1006/taap.1996.8029

Milhas, D., C.J. Clarke, J. Idkowiak-Baldys, D. Canals, and Y.A. Hannun. 2010. Anterograde and retrograde transport of neutral sphingomyelinase-2 between the Golgi and the plasma membrane. *Biochim. Biophys. Acta*. 1801:1361–1374.

Murshed, M., T. Schinke, M.D. McKee, and G. Karsenty. 2004. Extracellular matrix mineralization is regulated locally; different roles of two gla-containing proteins. *J. Cell Biol.* 165:625–630. doi:10.1083/jcb.200402046

Murshed, M., D. Harmey, J.L. Millán, M.D. McKee, and G. Karsenty. 2005. Unique coexpression in osteoblasts of broadly expressed genes accounts for the spatial restriction of ECM mineralization to bone. *Genes Dev.* 19:1093–1104. doi:10.1101/gad.1276205

Nesbitt, T., I. Fujiwara, R. Thomas, Z.S. Xiao, L.D. Quarles, and M.K. Drezner. 1999. Coordinated maturational regulation of PHEX and renal phosphate transport inhibitory activity: evidence for the pathophysiological role of PHEX in X-linked hypophosphatemia. *J. Bone Miner. Res.* 14:2027–2035. doi:10.1359/jbmr.1999.14.12.2027

Obeid, L.M., C.M. Linardic, L.A. Karolak, and Y.A. Hannun. 1993. Programmed cell death induced by ceramide. *Science*. 259:1769–1771. doi:10.1126/science.8456305

Okawa, A., I. Nakamura, S. Goto, H. Moriya, Y. Nakamura, and S. Ikegawa. 1998. Mutation in Npps in a mouse model of ossification of the posterior longitudinal ligament of the spine. *Nat. Genet.* 19:271–273. doi:10.1038/956

Richard, A., S. Bourgoin, P.H. Naccache, G.P. L'Heureux, E. Krump, S.R. McColl, and G. Pelletier. 1996. C2-ceramide primes specifically for the superoxide anion production induced by N-formylmethionylleucyl phenylalanine (fMLP) in human neutrophils. *Biochim. Biophys. Acta*. 1299:259–266.

Rossert, J., H. Eberspaecher, and B. de Crombrugghe. 1995. Separate cis-acting DNA elements of the mouse pro-α1(I) collagen promoter direct expression of reporter genes to different type I collagen-producing cells in transgenic mice. *J. Cell Biol.* 129:1421–1432. doi:10.1083/jcb.129.5.1421

Rutkute, K., R.H. Asmis, and M.N. Nikolova-Karakashian. 2007. Regulation of neutral sphingomyelinase-2 by GSH: a new insight to the role of oxidative stress in aging-associated inflammation. *J. Lipid Res.* 48:2443–2452. doi:10.1194/jlr.M700227-JLR200

Sanchez-Alavez, M., I.V. Tabarean, M.M. Behrens, and T. Bartfai. 2006. Ceramide mediates the rapid phase of febrile response to IL-1beta. *Proc. Natl. Acad. Sci. USA*. 103:2904–2908. doi:10.1073/pnas.0510960103

Stoffel, W., B. Jenke, B. Blöck, M. Zumbansen, and J. Koebke. 2005. Neutral sphingomyelinase 2 (smpd3) in the control of postnatal growth and development. *Proc. Natl. Acad. Sci. USA*. 102:4554–4559. doi:10.1073/pnas.0406380102

Stoffel, W., B. Jenke, B. Holz, E. Binczek, R.H. Günter, J. Knifka, J. Koebke, and A. Niehoff. 2007. Neutral sphingomyelinase (SMPD3) deficiency causes a novel form of chondrodysplasia and dwarfism that is rescued by Col2A1-driven smpd3 transgene expression. *Am. J. Pathol.* 171:153–161. doi:10.2353/ajpath.2007.061285

Tanaka, Y., and H.F. Deluca. 1974. Role of 1,25-dihydroxyvitamin D3 in maintaining serum phosphorus and curing rickets. *Proc. Natl. Acad. Sci. USA*. 71:1040–1044. doi:10.1073/pnas.71.4.1040

Tellier, E., A. Nègre-Salvayre, B. Bocquet, S. Itohara, Y.A. Hannun, R. Salvayre, and N. Augé. 2007. Role for furin in tumor necrosis factor alpha-induced activation of the matrix metalloproteinase/sphingolipid mitogenic pathway. *Mol. Cell. Biol.* 27:2997–3007. doi:10.1128/MCB.01485-06

Terkeltaub, R.A. 2001. Inorganic pyrophosphate generation and disposition in pathophysiology. *Am. J. Physiol. Cell Physiol.* 281:C1–C11.

Waymire, K.G., J.D. Mahuren, J.M. Jaje, T.R. Guilarte, S.P. Coburn, and G.R. MacGregor. 1995. Mice lacking tissue non-specific alkaline phosphatase die from seizures due to defective metabolism of vitamin B-6. *Nat. Genet.* 11:45–51. doi:10.1038/ng0995-45

Whyte, M.P. 1994. Hypophosphatasia and the role of alkaline phosphatase in skeletal mineralization. *Endocr. Rev.* 15:439–461.

Wu, B.X., C.J. Clarke, and Y.A. Hannun. 2010. Mammalian neutral sphingomyelinases: regulation and roles in cell signaling responses. *Neuromolecular Med.* 12:320–330. doi:10.1007/s12017-010-8120-z